Analysis of the Directivity of Glass-Etalon Fabry–Pérot Ultrasound Sensors

Danny R. Ramasawmy⬤, Eleanor Martin⬤, James A. Guggenheim⬤, Edward Z. Zhang,
Paul C. Beard, Bradley E. Treeby⬤, and Ben T. Cox⬤

Abstract—**Planar glass-etalon Fabry–Pérot (FP) optical ultrasound sensors offer an alternative to piezoelectric sensors for the measurements of high-intensity focused ultrasound (HIFU) fields and other metrological applications. In this work, a model of the frequency-dependent directional response of the FP sensor was developed using the global matrix method, treating the sensor as a multilayered elastic structure. The model was validated against the experimentally measured directional response of an air-backed cover-slip FP sensor with well-known material properties. In addition, the model was compared with the measurements of an all-hard-dielectric sensor suitable for HIFU measurements. The model was then used to calculate modal dispersion curves for both glass-etalon sensors, allowing the features of the directional response to be linked to specific wave phenomena. The features in the directivity of the air-backed cover-slip sensor are due to guided Lamb waves. Symmetric Lamb modes give rise to regions of high sensitivity, whereas anti-symmetric modes cause regions of low sensitivity. For the all-hard-dielectric sensor, two features correspond to the water-substrate and water-spacer compressional and shear critical angles. A region of high sensitivity close to the shear critical angle is associated with a leaky-Rayleigh wave, which has a frequency-dependent phase speed. At higher frequencies, this feature is counteracted by a region of low sensitivity, which occurs when there is no difference in the vertical displacement of the mirrors forming the FP cavity. The model may be used to improve and optimize the design of FP sensors or could be used to assist with the accurate deconvolution of the directional response from array measurements in metrological and imaging applications.**

Index Terms—**Directivity, Fabry–Pérot (FP), guided waves, matrix methods.**

I. Introduction

THE Fabry–Pérot (FP) ultrasound sensor can detect ultrasound with high sensitivity over a broadband frequency range (tens of megahertz), with small element sizes (tens of micrometer). It is frequently used in photoacoustic imaging, as a reference sensor for hydrophone calibration, and it can also be used for general ultrasound field characterization [1]–[9]. A detailed comparison of the advantages and disadvantages of common FP sensors with other hydrophones can be found in [10]. The signals measured by the FP sensor, as with any ultrasound detector, are a function of both the acoustic signal and the system response of the sensor. The system response is dependent on both the frequency and the angle of the incident wave and so is termed the frequency-dependent directional response or directivity. When designing an ultrasound sensor for a particular application, the directional response is an important factor to take into consideration. For example, for accurate measurements of a highly focused acoustic field containing waves incident on the sensor at angles far from normal, it would be beneficial for the sensor to have an omnidirectional response. A directional response that varies significantly with angle may cause artifacts in the measurements. Conversely, there may be cases where having a highly directional response is desirable, for example, to minimize the detection of edge waves when measuring sound speed and absorption [11].

In general, there are two mechanisms which contribute to the directional response of a sensor. The first, which is common to all sensors, is due to spatial averaging. The significance of this effect is determined by the size of the detection area in comparison with the wavelength of the incident ultrasonic wave: the larger the detection area, the more directional the response. The second is dependent on the sensor construction and is due to the complex wave field produced from the multilayered structure of the sensor and from diffraction effects around the sensor. For a planar FP sensor interrogated by sufficiently small interrogation spot size, the complex wave field within the sensor will dominate the directional response. This is the principal mechanism investigated in this paper.

Many practical applications of planar FP ultrasound sensors have been successfully demonstrated [5], [8], [12], [13]. Beard and Mills [1] and Beard *et al.* [2] modeled the transduction mechanism for low-finesse FP interferometers consisting of thin-metallic mirrors and showed good agreement with the measured normal incidence frequency response. Weise *et al.* [14] modeled the response of an alternating stack of dielectric mirrors forming a thin high-finesse FP interferometer deposited on the tip of an optical fiber by combining a multilayered optical model [7], [15] with an acoustic finite element simulation. Weise *et al.* only investigated the normal incidence response of the fiber-optic sensor. After estimating the strain-optic coefficients of mirrors in the model, they showed good agreement with the measured normal incidence

TABLE I
TABLE OF MATERIAL PROPERTIES

Material	$c_l(ms^{-1})$	$c_s(ms^{-1})$	$\rho(kgm^{-3})$
Water [17]	1448	0	1000
Glass [17]	5570	3430	2500
SiO$_2$ [18]	5900	3700	2500
ZrO$_2$	-	-	5680
Air [17]	330	0	1
Aluminium [17]	6250	3100	2700

c_l, c_s: compressional and shear sound speeds, ρ : density.

frequency response. They also identified the acoustic modes, which affected the frequency response, showing that there were contributions from longitudinal, lateral, and Rayleigh waves as well as edge diffraction effects. Cox and Beard [4] extended the normal-incidence model of Beard *et al.* [2] to calculate the frequency-dependent directional response of a soft-polymer sensor. They used a three-layer elastic model (two half-spaces sandwiching the FP cavity), as the mirrors were acoustically negligible. The model showed good agreement with the measurements taken. However, the measurements exhibited a low signal-to-noise ratio of above 10 MHz, and the features were dominated by the effect of spatial averaging due to the large interrogation beam spot size. This precluded the observation of features that occur at high frequencies and large angles arising from complex wave-field interactions.

Unfortunately, the assumption that the mirrors are acoustically negligible is no longer reasonable when modeling FP sensors with mirrors made from many alternating dielectric materials. These sensors will be referred to as hard-dielectric FP sensors and show promise as a tool for measuring high-intensity ultrasound fields [3], [7], [10]. This paper extends the model of Cox and Beard [4] to this case. Two glass-etalon FP sensors are studied. First, an air-backed cover-slip sensor was used to validate the model to high frequencies (up to 100 MHz). Second, the directional response of an all-hard-dielectric FP sensor used for high-intensity focused ultrasound (HIFU) measurements in Martin *et al.* [10] was calculated and compared with measurements. The model was then used to analyze in detail how the various features in the directivity arise from wave modes in the sensor.

A brief description of the sensors' transduction mechanism and the acoustic model used to calculate the directional response is provided in Section II. Directivity measurements and comparisons to the model are given in Section III. Finally, the causes of the features present in the directional response are discussed in detail in Section IV.

II. MODEL OF FREQUENCY-DEPENDENT DIRECTIVITY

A. Transduction Mechanism and Directivity

As mentioned in Section I, two FP sensors were constructed. The air-backed cover-slip sensor was constructed from a glass microscope cover-slip with aluminum mirrors deposited either side. The cover-slip was mounted at the edges to a polycarbonate frame to allow the sensor to be easily secured in a water bath yet remain air-backed. The properties of the sensor materials can be found in Table I. The all-hard-dielectric FP
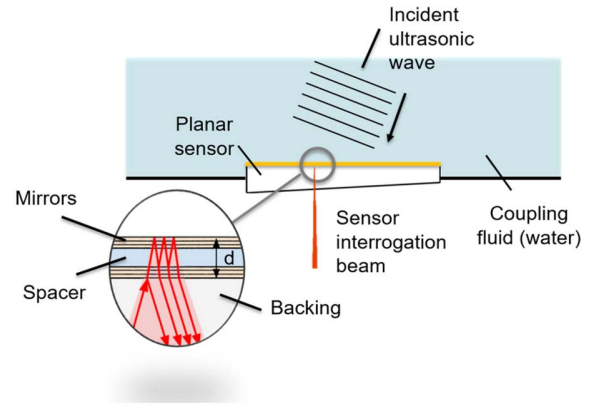

Fig. 1. Schematic of an all-hard-dielectric FP interferometer. Two dielectric mirrors separated by a SiO$_2$ spacer (with a combined thickness of d) are deposited onto a wedge-shaped glass substrate. The sensor is interrogated by a focused laser beam at the base of the substrate, where the wedge shape helps prevent parasitic interference [4]. The beam is multiply-reflected between the mirrors, and the reflected intensity is measured. An incident ultrasonic wave modulates the optical path length between the mirrors and the reflected intensity of the laser. The air-backed cover-slip sensor is supported by a polycarbonate frame and does not have a wedge-shaped substrate. In addition, the air-backed cover-slip has thin aluminum mirrors.

sensor consisted of two partially reflecting dielectric mirrors separated by a thin spacer deposited on a substrate, as shown in Fig. 1. The dielectric mirrors were constructed from 12 $\lambda/4$ thick alternating layers of silicon dioxide (SiO$_2$) and zirconium dioxide (ZrO$_2$) separated by a spacer made from SiO$_2$, where λ refers to the optical wavelength within the material.

With reference to Fig. 1, light from an interrogating laser beam is multiply-reflected between two mirrors separated by an optically transparent spacer layer. The intensity from the superposition of the multiply-reflected light wave fields is measured. In the presence of an acoustic wave, a change in the intensity of the reflected beam may arise from two mechanisms. The first is a path length change, as the distance between the mirrors is modulated by the acoustic wave. The second is due to a change in the refractive index of the materials caused by local changes in density associated with the acoustic wave.

The first mechanism is calculated by taking the difference in the vertical component of the displacement field u_z between the two mirrors. The second mechanism is calculated by integrating the changes in refractive index Δn over the spacer and mirror layers. Here, only refractive index changes in the spacer have been included, and any changes in the mirrors have been neglected. Assuming that the spacer material is optically isotropic, homogeneous, and non-absorbing the changes in refractive index can be written as

$$\Delta n = -\frac{1}{2}n_0^3 \left(p_{11}\frac{\partial u_x}{\partial x} + p_{12}\frac{\partial u_z}{\partial z} \right) \tag{1}$$

when the interrogating laser beam is parallel to z and polarized in x [3], [16]. When polarized in y, the strain-optic coefficient $p_{11} = p_{12}$.

The frequency-dependent directional response $D(f, \theta)$ to a plane wave of frequency f and angle of incidence θ can then be calculated by weighting the two mechanisms by the interrogation beam profile $S(x, y)$ and integrating over the

TABLE II
EFFECTIVE DIELECTRIC MIRROR PARAMETERS

Parameter	5-layer
Spacer thickness (μm)	3.885
Effective Thickness HD Mirror (μm)	1.40
Effective HD mirror c_l (ms^{-1})	4921
Effective HD mirror c_s (ms^{-1})	1930

interrogated area A

$$D(f, \theta) \propto \int_A [n_0(u_z(x, y; z_1) - u_{z_2}(x, y; z_2))$$
$$+ \int_{z_1}^{z_2} \Delta n.dz] S(x, y) dA. \quad (2)$$

Here, the displacements are taken at the midpoints of each mirror layer.

B. Global Matrix Method

The global matrix method (GMM) describes elastic and visco-elastic wave propagation in multilayered media and is used to calculate the vertical displacement of the mirrors. A comprehensive review of this method can be found in [19].

The air-backed cover-slip sensor was modeled using three layers: water (coupling fluid), glass spacer (175 μm), and air backing. The aluminum mirrors (an estimated thickness of <100 nm) were assumed to be negligible, as they are much smaller than the shortest acoustic wavelength considered. The all-hard-dielectric sensor was modeled using five elastic layers: water (coupling fluid), two dielectric mirrors (estimated at 1.4 μm), SiO$_2$ spacer (3.885 μm), and glass backing. The surface dimensions of the air-backed cover-slip was 22 $\times$ 22 mm and 50 $\times$ 30 mm for the hard-dielectric sensor. These dimensions were not modeled, as each layer is assumed to be infinite in the xy plane. The properties of the materials can be found in Tables I and II. As the acoustic properties of thin films are not well-known or easy to measure, the multilayered structure of the dielectric mirror was considered as one layer with effective material properties for sound speed and density, as discussed in Section III. This approach is valid, as the shortest wavelength is much longer than the thickness of each individual dielectric layer [20].

As mentioned in Section II-A, the vertical displacement of each mirror is needed to calculate directivity. The well-known isotropic stress–strain relationship for elastic materials and strain tensor for small deformations can be combined to give the elastic wave equation for the vector particle displacement. This can, in turn, be written as two separate wave equations using the Helmholtz decomposition [17], [19]. These are given as

$$\frac{\partial^2 \phi}{\partial t^2} - c_l^2 \nabla^2 \phi = 0, \quad \frac{\partial^2 \boldsymbol{\psi}}{\partial t^2} - c_s^2 \nabla^2 \boldsymbol{\psi} = 0 \quad (3)$$

where c_l and c_s are the compressional and shear sound speed and ϕ and $\boldsymbol{\psi}$ are the scalar and vector potentials, respectively. The first equation describes compressional waves based on the scalar potential, and the second describes shear waves, where $\boldsymbol{\psi}$ points perpendicular to the displacement $\nabla \times \boldsymbol{\psi}$ and to the
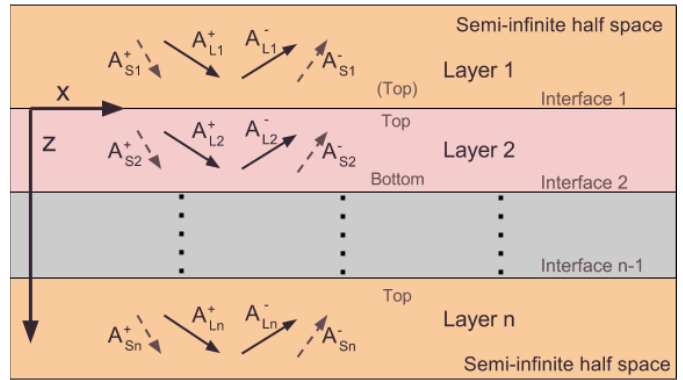

Fig. 2. Labeling notation for the GMM for a system of n-elastic layers, there are four bulk waves in each layer consisting of compressional (L, solid lines) and shear (S, dashed lines) waves traveling upward (−) or downward (+). The sum of one bulk wave type in a single layer is given by a complex amplitude A. The stress and the displacement, from the bottom and top of the interface of adjacent layers, must be continuous.

direction the wave travels. The model is simplified to 2-D by defining the vector potential as $\boldsymbol{\psi} = (0, \psi, 0)$, where ψ is a scalar [4]. This constrains the shear wave propagation to be only vertically polarized in the plane (x, z), thus excluding the out-of-plane motion of horizontally polarized shear waves and Love modes. This is not a limitation, as, by definition, horizontally polarized shear waves will not affect the vertical displacement of the sensor and, therefore, will not affect the directional response. The resulting displacement vector is

$$\mathbf{u} = \left(\frac{\partial \phi}{\partial x} - \frac{\partial \psi}{\partial z}, 0, \frac{\partial \phi}{\partial z} + \frac{\partial \psi}{\partial x} \right). \quad (4)$$

Plane wave solutions to (3), at a single frequency, take the form $\phi = A_L \exp\{i(\mathbf{k} \cdot \mathbf{x} - \omega t)\}$ and $\psi = A_S \exp\{i(\mathbf{k_t} \cdot \mathbf{x} - \omega t)\}$, where A_L and A_S are the complex compressional and shear wave amplitudes, $\mathbf{k}$ and $\mathbf{k_t}$ are the compressional and shear wavenumber vectors, and ω is the circular frequency. The stress and displacement within each layer of the FP sensor can be found from the superposition of the acoustic fields from four bulk waves. These are upward and downward traveling longitudinal and shear waves, as shown in Fig. 2.

The 2-D model requires four boundary conditions to be met at the interfaces between two adjacent elastic layers. For perfectly bonded elastic layers, the normal σ_{zz} and shear σ_{xz} stress and the normal u_z and transverse u_x displacement must be continuous across the interface [19]. Therefore, there are four equations for every interface in the system. At a fluid–solid interface, there are only three boundary conditions, as there is no continuity of transverse displacement.

The equations for an n-layered structure can be assembled into a single (global) matrix, which consists of $4(n - 1)$ equations and $4n$ unknown wave amplitudes A [19]. For example, a five-layer model will take the form

$$\begin{bmatrix} D_{1,b} & -D_{2,t} & & & \\ & D_{2,b} & -D_{3,t} & & \\ & & D_{3,b} & -D_{4,t} & \\ & & & D_{4,b} & -D_{5,t} \end{bmatrix} \begin{bmatrix} A_1 \\ A_2 \\ A_3 \\ A_4 \\ A_5 \end{bmatrix} = 0. \quad (5)$$

Here, each $D_{i,j}$ is a 4×4 field matrix at interface i from the top t or bottom b side of the interface. Each A_k is a 4×1 vector of the complex compressional and shear bulk wave amplitudes in layer k. To ensure that the matrix is well-conditioned, the rows of the field matrices and the corresponding components of A relating to displacement continuity are scaled by the incident wavenumber of the first layer, and the rows relating to stress continuity are scaled by $\rho\omega^2$. Knowledge of four of the bulk wave amplitudes A allows the system to be rearranged and solved for the remaining amplitudes. Since water can only support a compressional wave and there are no waves traveling in the negative z-direction of the substrate backing, three of the wave amplitudes in the half-spaces $\left(A_{S1}^+, A_{Ln}^-, A_{Sn}^-\right.$ in Fig. 2) are set to zero. In addition, the wave amplitude for the incident compressional wave in water A_{L1}^+ can be set to 1 without loss of generality.

After solving for the bulk wave amplitudes, the complex displacement at the mirrors can be calculated from (4). Additional information, such as the complex reflection coefficient, can be calculated by taking the ratio of the reflected wave amplitude and incident wave amplitude, $R = A_{L1}^-/A_{L1}^+$. By introducing either a complex wavenumber or complex sound speed, absorption can be defined for individual layers. This can be helpful when trying to identify leaky-wave modes [20]. The guided wave modes can be determined by extracting the dispersion curves from the model [19]. These dispersion curves are obtained by finding the frequency-angle or frequency-wavenumber pairs at which the determinant of the global system matrix [see (5)] is singular. Practically, this is achieved by choosing one angle or wavenumber and by evaluating the determinant of the system matrix over a coarse range of frequencies. The determinant will tend to zero at frequencies close to modal solutions. A bisection algorithm can then be used to find the exact frequency where the matrix is singular. This process can be repeated over the desired range of angles or wavenumbers [19].

III. DIRECTIVITY MEASUREMENTS

A. Experimental Methods

As a validation, the model was initially compared with the directivity measurements of the air-backed cover-slip sensor. This has well-known material properties and many features in its directional response. However, such a sensor is rarely useful in applications, and therefore, a comparison of the model was also made with the more practical all-hard-dielectric sensor presented by Martin *et al.* [10]. The measurements were made using the method described by Guggenheim *et al.* [21]. This is briefly described here, and more details can be found in [21].

The FP sensor was mounted within the base of a specially designed water bath suspended above the optics required for the interrogation of the sensor, as shown in Fig. 3. A monopolar broadband (up to 100 MHz) plane wave photoacoustic source attached to a rotating stage was moved at $0.25°$ intervals about the point of interrogation on the surface of the FP sensor. The diameter of the plane wave source was 2.5 cm. A focused laser beam, which had an interrogation spot size of 25 μm and was tunable in the range of 1440–1640 nm
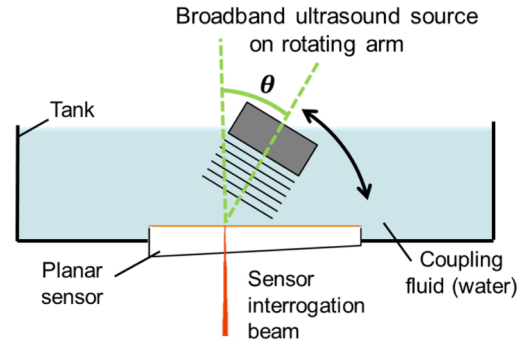

Fig. 3. FP sensor is placed at the base of a bath of deionized water. A broadband laser-generated ultrasound source is attached to a moveable stage, which rotates at $0.25°$ increments about the interrogation point on the surface of the FP sensor.

(Tunics T100S-HP, Yenista Optics, Lannion, France), was used to interrogate the FP sensor at an acquisition rate of 20 Hz. This was the maximum pulse repetition frequency of the photoacoustic source. Signals were acquired with 200 and 25 averages for the air-backed cover-slip sensors and hard-dielectric sensor, respectively. The measured time series were Fourier transformed and normalized by the normal-incidence frequency response to give the frequency-dependent directional response of the FP sensor.

B. Validation With Air-Backed Glass Cover-Slip

The model of the frequency-dependent directional response was validated by comparing it with measurements made with the air-backed cover-slip sensor. Fig. 4(a)–(c) shows the measured and modeled directional response between $\pm40°$ and $0-45$ MHz. To remove the effect of the frequency dependence of the photoacoustic source, the measured data in Fig. 4(a)–(c) were normalized so that the magnitude of the normal-incidence frequency response matched the modeled frequency response, as shown in Fig. 4(d).

Fig. 4(b) and (c) shows the modeled directivity with and without refractive index changes. The differences due to including the refractive index changes are smaller than the uncertainty in the measurement. In Section IV, the features in the directional response are sufficiently described by considering only the difference in the vertical displacement of the two mirrors. In addition, the strain-optic coefficients are not known or easily measured for thin-film dielectric mirrors and add further uncertainty in the modeling of the all-hard-dielectric sensor [14]. For this study, it was decided to neglect contributions from refractive index changes in Figs. 5–13.

The air-backed cover-slip is thick (≈175 μm) when compared with the shortest acoustic wavelength supported by the incident wave. At resonant frequencies, there is constructive or destructive interference within the cover-slip, which cause peaks and nulls in the frequency response. At normal incidence, the resonant peaks occur when $n\lambda + \lambda/2$ is equal to the cover-slip thickness, where $n = 0, 1, 2, 3\ldots$ and λ is the acoustic wavelength within the cover-slip. The peaks can be seen at 16, 47, and 79 MHz in Fig. 4. The nulls occur when $n\lambda$
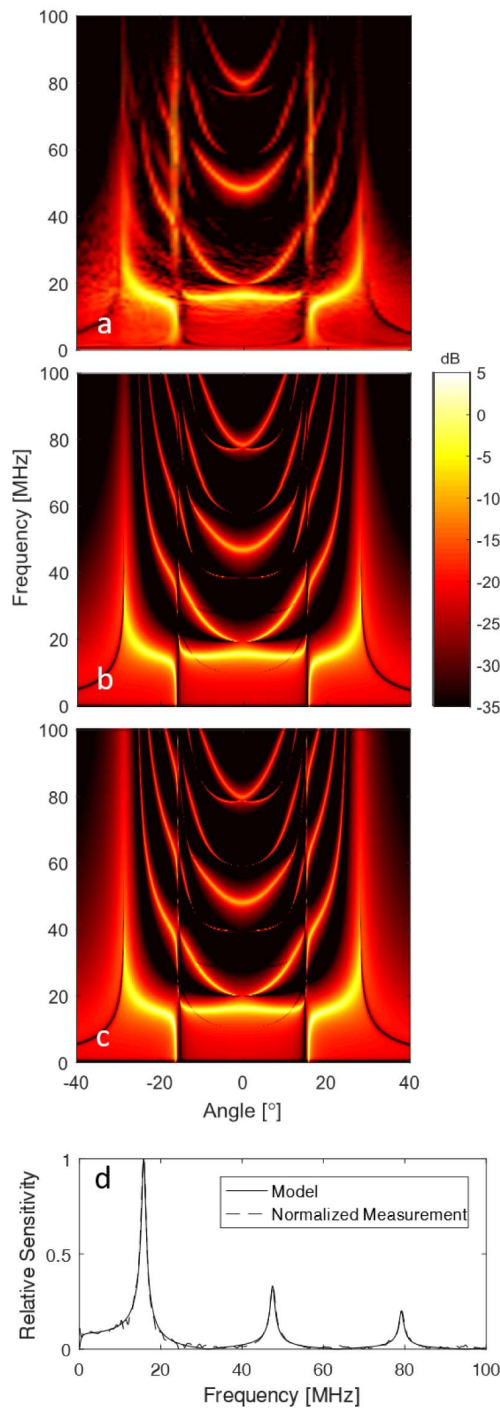
Fig. 4. (a) Measured directivity in decibels of the air-backed cover-slip sensor. The measurements were taken at 0.25° intervals using a photoacoustic signal generated by a 40-mJ laser pulse with 200 averages acquired between −40° and 40°. (b) Modeled directivity excluding refractive index changes and (c) modeled directivity including refractive index changes, where $p_{11} = 0.113$ and $p_{12} = 0.23$ [22]. Both the measured and modeled directivities have been normalized by the maximum of the first peak in the normal-incidence frequency response. (d) Model excluding refractive index changes (solid line) and normalized measurement (dashed line) of the normal-incidence frequency response.

is equal to the cover-slip thickness. There are nulls at 31, 62, and 94 MHz. At non-normal angles of incidence, there are a variety of features, which can be best seen in Fig. 5 which shows horizontal profiles through the directivity colormap.
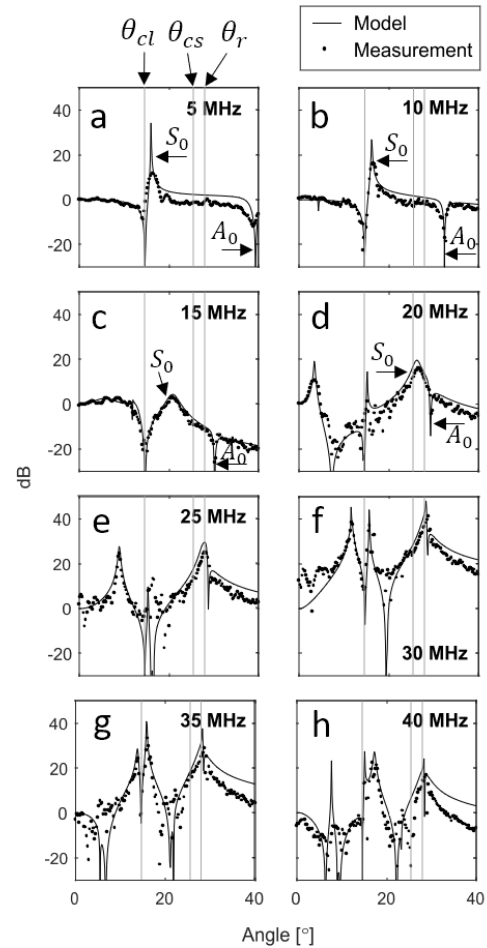

Fig. 5. One-sided profiles of the air-backed sensor at 5-MHz intervals up to 40 MHz of the measured (points) and modeled (line) directivity normalized to the normal-incidence frequency response. Note the vertical axis is in decibels.

These arise from critical angles and guided wave phenomena and will be described in more depth in Section IV.

C. Hard-Dielectric Sensor

The model was used to help interpret and explain the features of the directional response of a hard-dielectric sensor recently used for measuring the field generated by an HIFU transducer [10]. However, the acoustic properties of the dielectric mirrors used in this sensor are not known. To overcome this, effective material properties were found by fitting the model to the measured directional response of the HD sensor.

The dielectric mirrors consisted of 12 alternating layers of vapor-deposited SiO_2 and ZrO_2. Over the measurement bandwidth, the shortest acoustic wavelength is much larger than the thickness of any individual layer in the dielectric mirror. Therefore, the multilayered mirror structure was modeled as a single layer with effective acoustic properties for thickness, compressional sound speed, and shear sound speed. The material parameter fitting was performed using the `globalsearch` and `fmincon` functions from the Global Optimization Toolbox in MATLAB. These functions were used to minimize the sum-of-squared differences (SSDs) between the measured and modeled directional responses by varying the model values for the compressional sound speed,
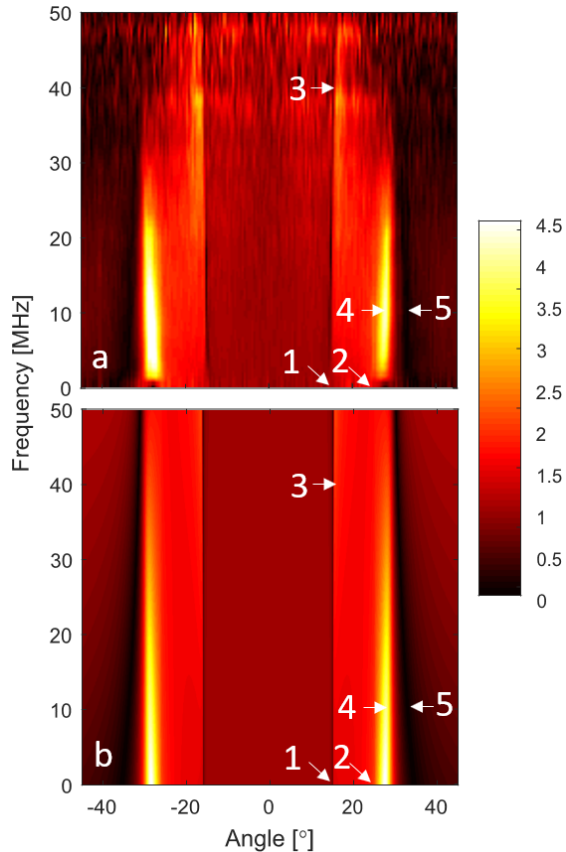
Fig. 6. (a) Directivity measurement of the hard-dielectric sensor presented by Martin *et al.* [10]. (b) Modeled directivity of the same sensor. Key features. 1: compressional critical angle. 2: shear critical angle. 3: peak after water-substrate and water-spacer compressional critical angles at high frequencies. 4: peak preceding Rayleigh wave with a frequency-dependent phase speed. 5: minimum due to no difference in the vertical displacements of the mirrors.
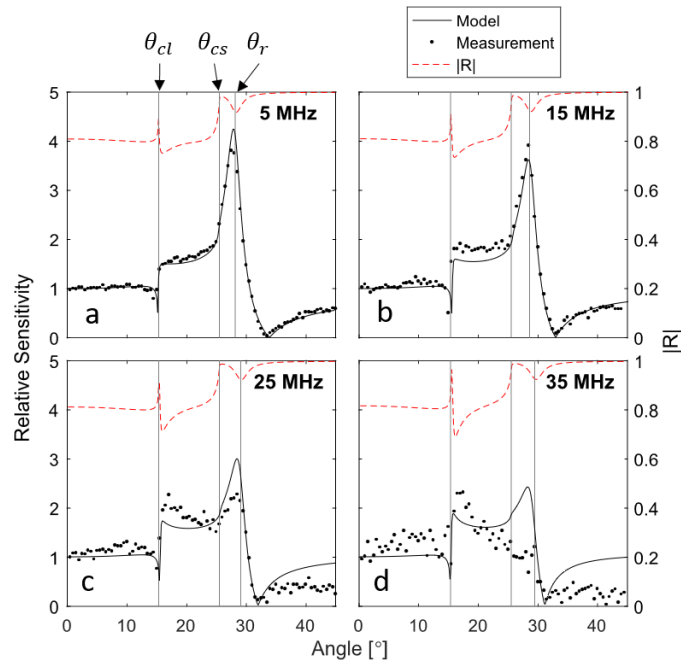

Fig. 7. One-sided profiles of the hard-dielectric sensor at (a) 5, (b) 15, (c) 25, and (d) 35 MHz of the measured (points) and modeled (solid line) directivity. The magnitude of the modeled reflection coefficient (red dashed line) at each frequency is plotted for reference. The left vertical axis is the relative sensitivity of the directional response profiles. The right vertical axis is the magnitude of the reflection coefficient. The vertical gray lines indicated on (a) represent the compressional critical angle θ_{cl} between water and glass, the shear critical angle θ_{cs}, and the leaky-Rayleigh angle θ_r.

the shear sound speed, and the thickness of the dielectric mirrors. The measured data were filtered using a low-pass filter (one-sided Gaussian, -3-dB point at 30 MHz) to regularize the inversion against high-frequency noise in the measurements. The implementation of the inversion routine was validated using both noise-free and noisy synthesized data. The values found for the estimated parameters are shown in Table II.

When using these fitted material properties, there is good agreement between the measured and modeled directional responses. Fig. 6(a) and (b) shows the magnitude of the measured and modeled directional response for the hard-dielectric sensor normalized to the normal-incidence frequency response. This is plotted between $\pm 45°$ for a range of frequencies from 0 to 45 MHz. The corresponding phase response is shown in Fig. 8. One-sided profiles of the directional response are shown in Fig. 7. The mirrors and spacer of the hard-dielectric sensor are thin (≈ 9 μm) when compared with the shortest wavelength present in the incident wave, resulting in a flat frequency response.

IV. FEATURE ANALYSIS

A. Overview

In Section III, the model was validated by comparing it with directional response measurements, but the responses

themselves were not analyzed in terms of the underlying acoustic wave interactions. The key features of the directional responses for the hard-dielectric and air-backed cover-slip sensors have been labeled in Figs. 6 and 10 and will be discussed in detail in Sections IV-B–IV-D. Generally, the features of the directional response can be associated with wave phenomena in the sensor. For example, features which occur over a narrow angular range for every frequency appear as vertical bands in the directional response and are associated with compressional and shear critical angles. Also, maxima occur when the incident wave couples into symmetric Lamb waves or Rayleigh waves, and minima may occur from anti-symmetric Lamb waves or other cases when both mirrors are moving in phase and have the same displacement.

B. Critical Angles

1) Hard-Dielectric Sensor: In general, the acoustic wave incident on the FP sensor couples into both compressional and shear waves. These effects are more apparent on the directivity of the hard-dielectric sensor, and hence, this is discussed first. At the water-substrate compressional critical angle ($\theta_{cl} = 15.4°$), there is only an evanescent compressional wave, which travels perpendicular to the substrate. The vertical displacement of the evanescent mode decays exponentially from the water-mirror interface into the substrate. At low frequencies, the wavelength is large compared with the thickness of the mirrors and spacer, and both mirrors have a similar displacement. As there is no significant difference in displacement between the two mirrors, there is a null in the
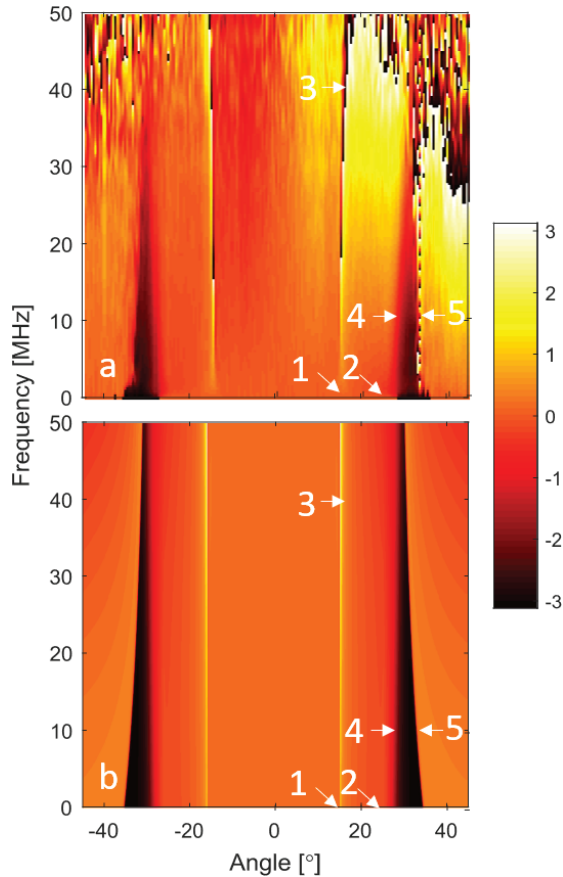
Fig. 8.   (a) Phase response of the directivity measurement presented by Martin *et al.* [10] and (b) modeled phase response of the hard-dielectric sensor. Key features. 1: compressional critical angle. 2: shear critical angle. 3: peak after water-substrate and water-spacer compressional critical angles at high frequencies. 4: peak preceding Rayleigh wave with a frequency-dependent phase speed. 5: minimum due to no difference in the vertical displacements of the mirrors.
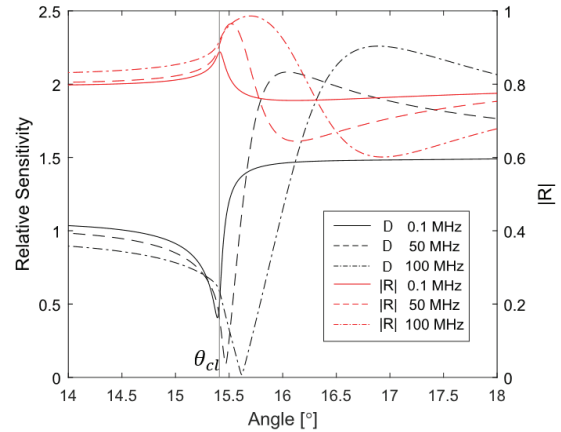

Fig. 9.   Critical angle separation in the hard-dielectric sensor. The modeled directivity and reflection coefficient have been plotted at three frequencies over a narrow angular range near the compressional critical angle between water and glass. The left vertical axis indicates the relative sensitivity of the directional response, and the right vertical axis indicates the magnitude of the reflection coefficient. The gray vertical line indicates the critical angle between glass and water. A dip in the directional response is associated with the first critical angle and moves from $15.4°$ to $15.7°$, as the peak in the reflection coefficient broadens.

sensitivity. This can be more clearly observed when looking at profiles of the directivity, as shown in Fig. 7(a)–(d). Here, one-sided profiles of the directivity have been plotted at four frequencies. The modeled reflection coefficient $|R|$ has also been plotted as a reference commonly used in this type of analysis. There is a lack of sensitivity at the compressional critical angle and a corresponding peak in $|R|$. This is also the cause of the vertical banding features in Fig. 6 and a change in phase seen in Fig. 8 (1).

The compressional critical angle feature is frequency-dependent due to the increasing significance of the thin mirror and spacer layers at shorter wavelengths. Considering individual plane waves of different frequencies incident on the sensor, long wavelengths will only "see" the bulk sound speed of the substrate. However, for shorter wavelengths, the effective sound speed will be a combination of the spacer, the mirrors, and the substrate, and there may be multiple compressional critical angles. This can be seen in Fig. 7. As the frequency increases from 5 to 35 MHz, there is a broadening of both the critical angle dip and reflection coefficient peak. This is further shown in Fig. 9, which shows the modeled directivity and

reflection coefficient for three frequencies over a small angular range between $14°$ and $18°$. As the frequency changes from 0.1 to 100 MHz, the dip in the directional response associated with the compressional critical angle moves from $15.4°$ to $15.7°$.

Immediately, following the compressional critical angle, there is strong mode conversion into the shear mode. Less of the incident wave energy is reflected causing an increase in the magnitude of the displacements of the mirrors. This corresponds to a small peak in directivity, which can be seen in Fig. 6(a) and (b) (3).

After the shear critical angle $\theta_{cs} = 25°$, the incident wave couples into an evanescent wave, which decays exponentially from the surface. The surface displacement increases, as the incident wave starts to couple into the leaky-Rayleigh mode at θ_r and decreases after. This can be seen as a rapid increase in sensitivity in Fig. 7(a)–(d) following the water-substrate shear critical angle when the reflection coefficient approaches unity. There is also a dip in the reflection coefficient after the shear critical angle. This is a result of adding a small value of attenuation to the model to help visually identify when the Rayleigh wave occurs. With no attenuation in the model, a leaky-Rayleigh wave is still present but all the energy from the Rayleigh wave is re-emitted into the coupling fluid, and hence, the magnitude of the reflection coefficient is equal to unity. By including absorption, some of the energy of the Rayleigh wave is absorbed, and hence, the reflection coefficient is less than unity [23].

2) Air-Backed Cover-Slip Sensor: Like the hard-dielectric sensor, the air-backed cover-slip sensor has a minimum directional response at the compressional critical angle. This can be seen in the directivity profiles for the air-backed sensor in Fig. 5. These have been plotted between $0°$ and $40°$ at 5-MHz intervals up to 40 MHz. The additional peaks and
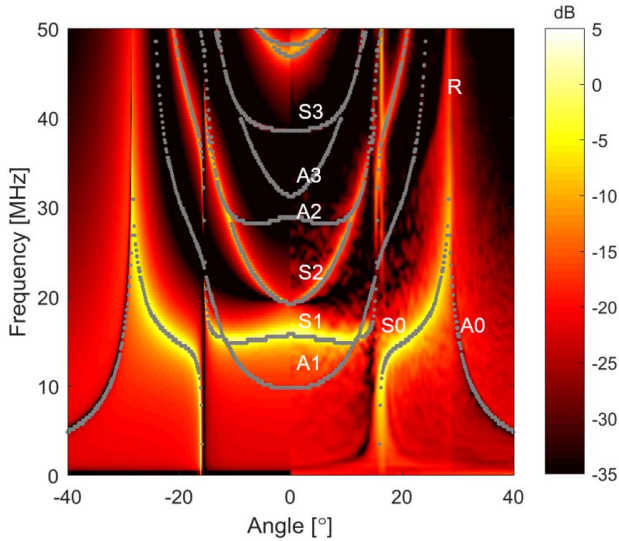
Fig. 10. Modeled directivity between $-40°$ and $0°$ and measured directivity between $0°$ and $40°$ from 0 to 50 MHz for the air-backed cover-slip sensor. The color scale has been plotted in decibels. The calculated dispersion curves have been plotted in gray and identified as symmetric (S) and anti-symmetric (A) Lamb modes and the Rayleigh mode (R). The guided wave modes that present in the sensor cause a complex directional response.

troughs, which can be seen in the profiles, are a result of Lamb modes and will be discussed in Section IV-C1.

C. Guided Wave Features

1) Lamb Waves: The majority of the observable features of the air-backed cover-slip arise from the incident wave coupling energy into leaky-Lamb modes. Generally, the sensor has a low sensitivity at frequencies and angles where the incident wave couples into the anti-symmetric mode. At frequencies and angles where the incident wave couples into symmetric Lamb modes, the sensor has a high sensitivity. Fig. 10 shows the dispersion curves for the glass plate over the directivity. These have been labeled anti-symmetric (A), symmetric (S), and Rayleigh (R).

For anti-symmetric mode shapes, the vertical displacement at the top and bottom of the sensor is the same. As there is no change in the distance between the two mirrors, there is a null in the sensitivity. For a symmetric mode, the vertical displacements at the top and bottom of the sensor have the same magnitude but in opposite directions. This opposing movement results in the maximum difference in vertical displacement and thus a high sensitivity. For frequencies and angles that do not couple into a Lamb mode, the displacement of the top and bottom surfaces will be somewhere between the symmetric and anti-symmetric modes, and hence, there is a gradual change in sensitivity between different modes. The mode shapes for the first- and second-order symmetric and anti-symmetric modes are plotted in Fig. 11 (a)–(d). Fig. 11 (e) and (f) demonstrates the shape of the glass cover-slip for the second-order symmetric and anti-symmetric modes, and the displacement has been exaggerated for visualization.

At normal incidence, the frequencies at which higher order Lamb modes begin can be calculated as the resonant frequencies of the glass cover-slip. For a 175-μm-thick
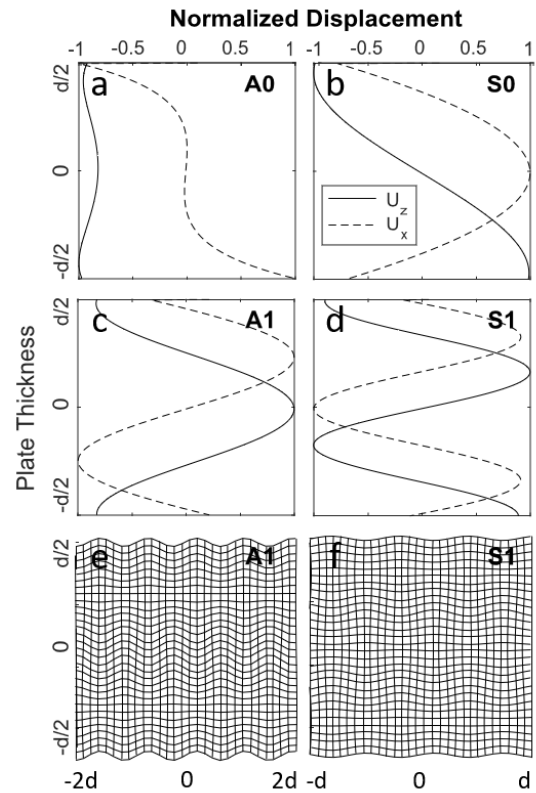

Fig. 11. (a)–(d) First- and second-order mode shapes of the symmetric and anti-symmetric Lamb waves present in the air-backed cover-slip sensor. The vertical (solid line) and transverse (dashed line) displacements across the thickness of the plate d have been plotted and normalized by the maximum displacement. For anti-symmetric modes, the displacement at the top of the glass cover-slip is the same as the bottom. For symmetric modes, the displacement at the top and bottom of the glass plate is out of phase. (e) and (f) Visualization of the symmetric and anti-symmetric mode shapes.

cover-slip, the resonances from a compressional mode occur at approximately 16, 31, and 47 MHz and from shear mode at 10, 19, 29, and 48 MHz, which can be seen in Fig. 10. The lowest-order Lamb waves, S0 and A0, can be seen from the lowest frequencies and couple into the leaky-Rayleigh mode. The fundamental Lamb modes have been labeled in Figs. 10 and 5(a)–(d). The Rayleigh mode is a common feature of both the hard-dielectric sensor and the air-backed cover-slip and will be discussed in Section IV-C2.

2) Leaky-Rayleigh Wave: Both the hard-dielectric and the air-backed cover-slip sensors have a feature of high sensitivity associated with a leaky-Rayleigh wave. The Rayleigh wave has an elliptical motion with the greatest displacement at the surface. As there is a large displacement at the surface, there is a difference in the vertical displacement between the mirrors causing a region of high sensitivity. This can be seen as a peak in the directivity that occurs immediately preceding the leaky-Rayleigh angle θ_r, which is labeled in Figs. 7(a)–(d) and 6 (4) for the hard-dielectric sensor. This can also be seen for the cover-slip sensor after the A0 and S0 Lamb modes couple [see Figs. 5(e)–(h) and 10 (R).

The leaky-Rayleigh wave for the air-backed cover-slip has a frequency-independent phase speed, as the sensor is primarily constructed from a single material. The Rayleigh speed of glass is 3152 ms^{-1}, which can be found using the
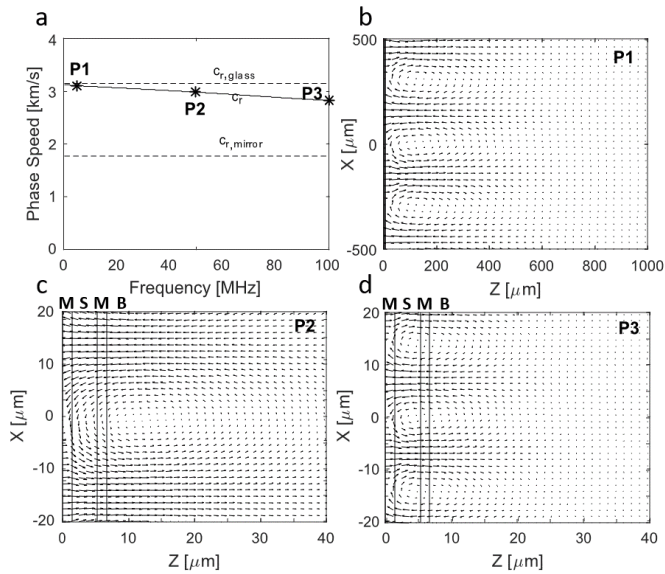
Fig. 12. Rayleigh wave plots generated for the hard-dielectric sensor. (a) Leaky-Rayleigh wave phase speed (solid line) with frequency. The Rayleigh speed for the glass substrate and the mirrors is also plotted (dashed line). (b)–(d) Vector field plots at three points on (a). The horizontal axis represents the depth from the water-mirror interface in μm, and the vertical axis is the position parallel to the interface. The vertical lines indicate the boundary between the mirror (M), spacer (S), and mirror-backing (B). The vertical lines cannot be seen on (b) over the plotted depth.
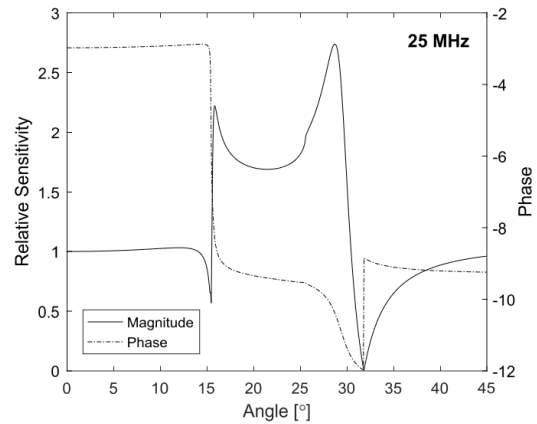

Fig. 13. Relative sensitivity at 25 MHz for the hard-dielectric sensor. The solid line represents the magnitude of the difference in the complex mirror displacements, and the dashed line indicates the phase. The minimum at 32° occurs when the mirrors have both the same absolute displacement and are in phase.

approximation $c_r/c_s = (0.862 + 1.14\nu)/(1 + \nu)$ [24], where ν is the Poisson's ratio of the material.

The hard-dielectric sensor has multiple elastic layers and the Rayleigh wave exhibits a frequency-dependent phase speed, as shown in Fig. 12(a). The Rayleigh wave speed is generally close to the bulk shear speed of the material that is traveling in. At low frequencies, the wavelength of the leaky-Rayleigh wave is much larger than the spacer and the mirrors, and the majority of the wave motion occurs in the substrate [see Fig. 12(b)]. At high frequencies, the wavelength is shorter, and more motion occurs within the spacer and the mirrors [see Fig. 12(c) and (d)]. The leaky-Rayleigh wave speed starts at that of the glass-substrate (3152 ms^{-1}) and moves toward the Rayleigh speed of the mirrors and spacer (1780 ms^{-1}). The dispersion curve for the leaky-Rayleigh mode can be seen in Fig. 12(a). At even higher frequencies (not shown here), higher order Rayleigh modes will appear [20], [25]. The displacement field plots, as shown in Fig. 12, also show elliptical motion for angles after the shear critical angle. However, the greatest sensitivity occurs at the Rayleigh angle when the surface displacement is a maximum. There is a gradual decrease in sensitivity after the Rayleigh angle.

D. Other Features

1) Low Sensitivity in the Hard-Dielectric Sensor: The peak in directivity associated with the leaky-Rayleigh wave is diminished by the crossing of the minimum highlighted in Fig. 6 (5). The displacement field within the sensor has an elliptical motion for angles larger than the shear critical angle. The depth of this motion into the sensor depends on the wavenumber component into the sensor (k_z). The value of

this component gets smaller for both a higher frequency and a larger angle of incidence. As the angle is increased from the shear critical angle, the depth of the elliptical motion becomes shallower. The displacements of the mirrors change from the top mirror having the larger displacement to the bottom mirror having the larger displacement. Through this transition, there is an angle where both mirrors will have the same magnitude and are moving in phase. Here, there is no difference in the vertical displacement between the top and bottom mirrors and is a null in the sensitivity. This is shown in Fig. 13, where the magnitude and phase profiles of the directional response are plotted at 25 MHz. The minimum can be seen at 32°. There is also a discontinuity in phase as the magnitude is zero and $a-\pi$ change in phase as the second mirror has the larger displacement.

V. Discussion

A. Model Limitations

The isotropic elastic multilayered model of the directional response of planar FP ultrasound sensors introduced in Section II agrees well with the measurements of directivity as discussed in Section III. However, it should be noted that this model may not be applicable to every FP ultrasound sensor. First, in this paper, the dominant transduction mechanism is considered to be the difference in the displacement of the two mirrors and neglects refractive index changes within the spacer and mirror layers due to the strain-optic effect. When including the change in refractive index for the spacer in the model of the directional response [see Fig. 4(c)], there were minimal changes in the directivity. In addition, the strain-optic coefficients are not well-known or easily measured for thin films. For other FP sensors, the strain-optic effect could contribute more significantly to the directional response. However, it does not affect the features in the directional response due to guided modes but could affect the amplitude response. Second, the model assumes that each elastic layer is infinitely long and planar and the model displacement is constrained to the (x, z) plane, which explicitly excludes

bulk horizontally polarized shear waves. Although horizontally polarized shear modes do not affect the vertical displacement of the mirrors, they may have an influence on the refractive index of the material, which may be important in materials with large strain-optic coefficients. Third, the model assumes that the materials used to construct FP sensors are isotropic. However, thinly deposited films may form anisotropic semi-crystalline structures, which would affect the phase speeds at which the guided waves would occur [26]. In these instances, this model may not accurately predict the directional response.

B. Model Applications

Knowledge of the physical mechanisms affecting the frequency-dependent directional response of the planar FP sensor can be used to inform the design of future sensors (see [4], [7]). For example, to increase the measurable bandwidth, the thickness of the spacer layer can be reduced. By ensuring that the spacer thickness is much lesser than the shortest wavelength to be measured, the sensor will have a relatively flat frequency response. The tradeoff to this is a reduction in sensitivity, as the displacement difference will be smaller for a thinner spacer compared with a thicker spacer of the same material. Reducing the spacer thickness will also move the guided wave features to higher frequencies. Another change that can be made to ameliorate the effect of guided wave features is to make the compressional and shear sound speeds of the sensor materials closer to the compressional wave speed of the coupling fluid. This will move critical angle features further from normal incidence. Indeed, when the sound speed of the sensor is less than that of the fluid, there will be no critical angle, giving the sensor a more omnidirectional response. For example, FP sensors consisting of a thin polymer spacer on a polymer backing material exhibit a flat frequency response with a few significant features in the directivity [21]. The tradeoff is that these sensors are less robust to high-intensity ultrasound.

VI. Summary

A model of the frequency-dependent directional response of planar glass-etalon FP ultrasound sensors was developed using the GMM treating the sensor as a multilayered elastic structure. The model was compared with the measurements made with an air-backed cover-slip and an all-hard dielectric sensor. The main features in the directivity were described as effects of physical wave phenomena, such as compressional and shear critical angles, Lamb modes, and Rayleigh modes. This model of the sensor directivity, and in particular of how it relates to the specific wave modes in the sensor, will not only inform future sensor design but could be useful when correcting array measurements for directivity effects.

References

[1] P. C. Beard and T. N. Mills, "Extrinsic optical-fiber ultrasound sensor using a thin polymer film as a low-finesse Fabry–Pérot interferometer," *Appl. Opt.*, vol. 35, no. 4, pp. 663–675, 1996.

[2] P. C. Beard, F. Pérénnes, and T. N. Mills, "Transduction mechanisms of the Fabry–Pérot polymer film sensing concept for wideband ultrasound detection," *IEEE Trans. Ultrason., Ferroelectr., Freq. Control*, vol. 46, no. 6, pp. 1575–1582, Nov. 1999.

[3] V. Wilkens, "Characterization of an optical multilayer hydrophone with constant frequency response in the range from 1 to 75 MHz," *J. Acoust. Soc. Amer.*, vol. 113, no. 3, pp. 1431–1438, Mar. 2003.

[4] B. T. Cox and P. C. Beard, "The frequency-dependent directivity of a planar Fabry–Pérot polymer film ultrasound sensor," *IEEE Trans. Ultrason., Ferroelectr., Freq. Control*, vol. 54, no. 2, pp. 394–404, Feb. 2007.

[5] E. Z. Zhang, J. Laufer, and P. Beard, "Backward-mode multiwavelength photoacoustic scanner using a planar Fabry–Pérot polymer film ultrasound sensor for high-resolution three-dimensional imaging of biological tissues," *Appl. Opt.*, vol. 47, no. 4, pp. 561–577, 2008.

[6] P. C. Beard, "Two-dimensional ultrasound receive array using an angle-tuned Fabry–Pérot polymer film sensor for transducer field characterization and transmission ultrasound imaging," *IEEE Trans. Ultrason., Ferroelectr., Freq. Control*, vol. 52, no. 6, pp. 1002–1012, Jun. 2005.

[7] V. Wilkens and C. Koch, "Fiber-optic multilayer hydrophone for ultrasonic measurement," *Ultrasonics*, vol. 37, no. 1, pp. 45–49, 1999.

[8] V. Wilkens and C. Koch, "Amplitude and phase calibration of hydrophones up to 70 MHz using broadband pulse excitation and an optical reference hydrophone," *J. Acoust. Soc. Amer.*, vol. 115, no. 6, pp. 2892–2903, Jun. 2004.

[9] K. Nakamura, *Ultrasonic Transducers: Materials and Design for Sensors, Actuators and Medical Applications*. Amsterdam, The Netherlands: Elsevier, 2012.

[10] E. Martin, E. Z. Zhang, J. A. Guggenheim, P. C. Beard, and B. E. Treeby, "Rapid spatial mapping of focused ultrasound fields using a planar Fabry–Pérot sensor," *IEEE Trans. Ultrason., Ferroelectr., Freq. Control*, vol. 64, no. 11, pp. 1711–1722, Nov. 2017.

[11] B. Zeqiri, W. Scholl, and S. P. Robinson, "Measurement and testing of the acoustic properties of materials: A review," *Metrologia*, vol. 47, no. 2, p. S156, 2010.

[12] E. Z. Zhang and P. C. Beard, "Broadband ultrasound field mapping system using a wavelength tuned, optically scanned focused laser beam to address a Fabry Pérot polymer film sensor," *IEEE Trans. Ultrason., Ferroelectr., Freq. Control*, vol. 53, no. 7, pp. 1330–1338, Jul. 2006.

[13] J. Laufer *et al.*, "*In vivo* photoacoustic imaging of mouse embryos," *J. Biomed. Opt.*, vol. 17, no. 6, 2012, Art. no. 061220.

[14] W. Weise, V. Wilkens, and C. Koch, "Frequency response of fiber-optic multilayer hydrophones: Experimental investigation and finite element simulation," *IEEE Trans. Ultrason., Ferroelectr., Freq. Control*, vol. 49, no. 7, pp. 937–946, Jul. 2002.

[15] H. A. Macleod, *Thin-Film Optical Filters*. Boca Raton, FL, USA: CRC Press, 2017.

[16] G. B. Hocker, "Fiber-optic sensing of pressure and temperature," *Appl. Opt.*, vol. 18, no. 9, pp. 1445–1448, 1979.

[17] J. L. Rose, *Ultrasonic Waves in Solid Media*, vol. 107. Cambridge, U.K.: Cambridge Univ. Press, 2004.

[18] R. Munro, "Elastic moduli data for polycrystalline oxide ceramics," Nat. Inst. Standard Technol., Gaithersburg, MD, USA, Tech. Rep. NISTIR-6853, 2002.

[19] M. J. S. Lowe, "Matrix techniques for modeling ultrasonic waves in multilayered media," *IEEE Trans. Ultrason., Ferroelectr., Freq. Control*, vol. 42, no. 4, pp. 525–542, Jul. 1995.

[20] D. B. Bogy and S. M. Gracewski, "On the plane wave reflection coefficient and nonspecular reflection of bounded beams for layered half spaces underwater," *J. Acoust. Soc. Amer.*, vol. 74, no. 2, pp. 591–599, 1983.

[21] J. A. Guggenheim, E. Z. Zhang, and P. C. Beard, "A method for measuring the directional response of ultrasound receivers in the range 0.3–80 MHz using a laser-generated ultrasound source," (in English), *IEEE Trans. Ultrason., Ferroelectr., Freq. Control*, vol. 64, no. 12, pp. 1857–1863, Dec. 2017.

[22] N. F. Borrelli and R. A. Miller, "Determination of the individual strain-optic coefficients of glass by an ultrasonic technique," *Appl. Opt.*, vol. 7, no. 5, pp. 745–750, 1968.

[23] J. Cheeke, *Fundamentals and Applications of Ultrasonic Waves*. Boca Raton, FL, USA: CRC Press, 2010.

[24] L. Freund, *Dynamic Fracture Mechanics*. Cambridge, U.K.: Cambridge Univ. Press, 1998.

[25] G. W. Farnell and E. L. Adler, "Elastic wave propagation in thin layers," in *Physical Acoustics*, W. P. Mason and R. N. Thurston, Eds. New York, NY, USA: Academic, 2012, ch. 2, pp. 35–127.

[26] G. E. Backus, "Long-wave elastic anisotropy produced by horizontal layering," *J. Geophys. Res.*, vol. 67, no. 11, pp. 4427–4440, 1962.